The orientation and strain dependence of dislocation structure evolution in monotonically deformed polycrystalline copper

Jun Jiang[1,2], T Ben Britton[2], Angus J Wilkinson[1]

1. Department of Materials, the University of Oxford, Park Road, Oxford, OX1 3PH, UK

2. Department of Materials, Imperial College London, Royal School of Mines, Exhibition Road, London SW7 2AZ, UK

This is a authors version of a publication in International Journal of Plasticity, Volume 69, June 2015, Pages 102–117 doi:10.1016/j.ijplas.2015.02.005

Abstract

The cross-correlation based HR-EBSD technique was used to derive stored geometrically necessary dislocation (GND) density in the OFHC copper samples deformed under uniaxial tension to true strain of 0%, 6%, 10%, 22.5% and 40%. Large maps (500μm x500μm with 0.5μm step size) with 1 million points and ~1600 grains were acquired at each deformation level. Detailed studies on dislocation structure and evolution using the HR-EBSD were conducted. Distinct types of dislocation arrangements were revealed in grains with various orientations. For example, dislocation cells were formed in grains of <110> orientation and dislocation bands were generally found in grains of <111> and <001> orientations. The complicated dislocation networks provide vital evidence to understand the deformation mechanisms in polycrystals at mesoscale. Quantitative analyses were also carried out to study this GND density orientation dependence in which Taylor factor was used as an indicator to quantify the grain resistance to deformation. It was found that points with high GND content preferentially accumulated in grains with high Taylor factor ('hard' grains) in deformed samples. This relation becomes stronger with increasing deformation.

Keywords:

Dislocation structure, orientation dependence, High resolution EBSD (HR-EBSD), geometrically necessary dislocation (GND) density

1. Introduction

Detailed understanding of the dislocation mechanisms in polycrystals during plastic deformation currently is still elusive in materials research community (Pokharel et al., 2014). For single crystals dislocation slip, interaction and accumulation are relatively well understood and discrete dislocation

models can clearly capture many observed dislocation features. For polycrystals satisfaction of geometrical compatibility and stress equilibrium between grains with various orientations lead to longer range patterning in dislocation storage which remains a long standing challenge to understand. The primary challenge is the large number of microstructural variables existing in polycrystal materials such as various grain orientations, different grain boundary types: twin boundary, low misorientation angle or high misorientation angle, triple junctions and so on. This requires a sufficient number of grains to be measured and analysed with detailed dislocation structures to be found in order to provide more insights into this problem.

The typically used techniques for dislocation density measurement are TEM and X-ray or neutron diffraction. However, the high spatial resolution TEM only probes rather relatively small areas where few grains can be observed (Fultz and Howe, 2012). The dependence of dislocation arrangements on grain orientations using the TEM technique on polycrystal copper and aluminium samples deformed under tension and compression was found by Huang et al (Huang and Winther, 2007) in 2007. The study was systematic, ~100 grains were selected with care and a series slices were cut to be examined in the TEM. Finally a 3D TEM dislocation network was reconstructed. As a result of TEM's high angular resolution, fine distinctions in various orientations were found. However, the commonly observed dislocation bands with large misorientation were neglected in their TEM study and the study of dislocation patterns near grain boundary were deliberately avoided. The HR-EBSD study presented here was aimed more toward characterising the influence grain boundaries and triple junctions have on perturbing the dislocation patterns.

Although X-ray diffraction can make dislocation measurement on significantly larger areas with deeper interaction volume, the relatively coarse spatial resolution associated with X-ray diffraction prohibits it from mapping fine dislocation structures (Guinier, 2013). Recent developments of high energy synchrotron X-ray beam has overcome this limit and been able to capture developed dislocation structures. However, using it to address the polycrystal plasticity problem and deal with the enormous statistical data are still ongoing (Als-Nielsen and McMorrow, 2011; Ice et al., 2005; Larson et al., 2002).

There is a growing body of evidence from DIC measurements (Abuzaid et al., 2012; Littlewood and Wilkinson, 2012b) that plastic strains are highly inhomogeneous at the microstructural length scale and that the patterns of high plastic strain regions span across many grains. Hence it is very important to capture deformation information on appropriate length scale.

Development of high resolution electron backscatter diffraction (HR-EBSD) by Wilkinson et al in 2006 has accomplished both high spatial and angular resolution (Wilkinson et al., 2006a; Wilkinson et al., 2006b). By measuring the EBSD pattern shifts using image cross-correlation method, relative residual stress and geometrically necessary dislocation (GND) density can be measured(Wilkinson and Randman, 2010a). This has successfully bridged the TEM and X-ray diffraction techniques and allows us to revisit the polycrystal plasticity problem with the hope of providing new evidence to further our understanding.

Recently many research works on polycrystal plasticity problems employing conventional EBSD have been conducted to study the GND density distributions as a function of strain level, grain orientation and Taylor factor in Al alloys, steels and Ni superalloys (Allain-Bonasso et al., 2012; Field et al., 2012). Due to the relatively low angular resolution of conventional EBSD analysis, the dislocation structure

was not revealed in lightly deformed specimens. A detailed comparison between the TEM technique and conventional EBSD systems on deformation structures in FCC materials was conducted by Mishin et al (Mishin et al., 2009) in 2009. They found that EBSD was unable to capture the dislocation boundaries with very low misorientation angles and hence this technique was only capable of studying dislocation boundaries with larger misorientation angles formed in heavily deformed samples. This prohibits the observation of dislocation development process. The lowest GND density readily detected by conventional EBSD has been assessed by various authors (Adams and Kacher, 2010; Chekhonin et al., 2014; Field et al., 2012) and is step size dependent. In copper at a 0.5μm step size GND density below 10^{14} m^{-2} cannot be determined using conventional EBSD (Adams and Kacher, 2010; Jiang et al., 2013b). Mishin et al (Mishin et al., 2009) suggested the emergence of HR-EBSD technique might provide promising deformation structure results for a much larger range of plastic deformation.

High angular resolution of the cross-correlation based EBSD analysis allows much improved GND density sensitivity (Wilkinson et al., 2006a). Fortunately issues with reference point selection that complicate extraction of absolute elastic strain values using HR-EBSD do not prevent GND analysis as only relative changes in crystal orientation are required and these do not depend on the specifics of the reference points. Littlewood et al using the HR-EBSD approach qualitatively investigated the stored GND density distributions in a titanium alloy deformed under tension (Littlewood et al., 2011) and fatigue (Littlewood and Wilkinson, 2012a). However the number of grains included in Littlewood's study was rather small (20-30). This was because data was collected at the full resolution of the EBSD camera which gave a relatively long exposure time per pattern (~1 second). Jiang et al (Jiang et al.2013b) examined the effects of detector binning and step size on GND density mapping and explored the competing effects on the sensitivity and speed of data acquisition and analysis. Greater binning of the detector results in shorter exposure time, allowing acquisition of a larger map in a given time but at lower measurement sensitivity. As the measured mean of GND density in 6% deformed sample is ~$10^{14.1}$ m^{-2}, selecting 4x4 binning is reasonable as this gives a GND measurement sensitivity of $10^{13.5}$ m^{-2}.

This paper follows our previous work on dislocation distributions and evolution in polycrystal copper deformed under tension (Jiang et al., 2013a). In that work, statistical analysis was carried out to establish that the GND density distribution can be accurately described by a log-normal probability function which scales with imposed plastic strain level. The sample averaged GND density increases with increasing plastic deformation and can be used as a single parameter to predict the flow stress according to the Taylor hardening model. GNDs were found to preferentially accumulate adjacent to some microstructure features such as the grain boundaries and triple junctions.

Furthermore, as Merriman et al measured GND density in pure aluminium samples deformed in channel die compression using conventional EBSD and reported that the development of GND density has strong orientation dependence (Merriman et al., 2008). Our study intends to further investigate the orientation dependent of GND structure.

The first aim of this current paper is to provide direct evidence on dislocation structure, their development with increasing plastic deformation and grain orientation dependence. A comparison with some previous TEM observations of dislocation structure will be made. The second aim is to determine if grain orientation affects the GND density stored in individual grains and how the

relationship changes with the increasing tensile strain. Taylor factor is used in this study to define the 'hard' and 'soft' grains.

2. Method

1.1 Mechanical test and EBSD

Five dog bone shaped OFHC (99.95% purity) polycrystal copper tensile specimens with gauge section of 25mm x 6mm x1.5mm were fabricated according to the ASM tensile test standard (Standard, 1996). These specimens were ground on silicon carbide papers from 250 grit to 2000 grit. Subsequently, they were polished with 1µm diamond paste and colloidal silica to have a mirror finish surface. The polished copper specimens were placed in a 550 ^{o}C (half of the melting point) pre-heated furnace for 15 minutes in order to allow the annealing process to reduce the residual stress and lower the dislocation density which had been induced during the manufacturing process. The formed oxidation layers as well as other free surface contaminations were removed by using an electro-polishing method in which the specimens were immersed in 85% phosphoric acid as an anode and a copper sheet was attached as cathode. An AA battery was used to supply 1.5 Volts potential difference in the circuit. The specimens were electro-polished for ~10 minutes with a removal rate of ~20µm per minute.

These five specimens were deformed to various uniaxial tensile (plastic) strain levels (0%, 6%, 10%, 22.5% and 40% respectively) at a strain rate of $2x10^{-6}$ s^{-1}. The strain was measured using the Lavision Strainmaster (http://www.lavision.de/) digital image correlation (DIC) technique. To minimise the induced cutting deformation, a Buehler Isomet 4000 Linear Precision slow saw was used to cut out the central gauge section from each tested specimen. These obtained samples were mounted on standard aluminium stubs and examined in a JEOL JSM 6500-F SEM. The crystallographic information was obtained using a TSL EBSD system. 20 KV accelerating voltage and ~17nA current were used to scan a 500µm x500µm area with a step size of 0.5µm. ~1600 grains with average grain diameter of ~10.5 um were included in the mapped area. High quality EBSD patterns (4x4 hardware binning, zero gain and zero black level) were recorded to 12 bit depth 225 pixel x 225 pixel images using a Digiview II camera.

As each map contains 1,000,000 points, saving all the EBSD pattern images into a single folder in Windows operating system gradually reduced the transferring frame rate from initially 16 frames per second to 2 frames per second. This problem was overcome by designing a Matlab software script (http://www.mathworks.co.uk/) to transfer and store all EBSD images into a single HDF5 file (http://www.hdfgroup.org/) (Jackson et al., 2014; Jiang et al., 2013b). This allowed the ~16 frames per second rate to be maintained throughout the data acquisition process.

1.2 HR-EBSD and GND density

To estimate the stored geometrically necessary dislocation (GND) density, the saved EBSD patterns were analysed using an image cross-correlation based software which had been developed in Matlab by the Authors (Britton and Wilkinson, 2011, 2012; Jiang et al., 2013b; Karamched and Wilkinson, 2010; Wilkinson et al., 2006a; Wilkinson et al., 2006b; Wilkinson and Randman, 2010b). This cross-correlation based method can improve the EBSD angular resolution to ~$1x10^{-4}$ rads or better (Wilkinson et al., 2006b). Though at the 4x4 binning used for these observations the angular

resolution is $5x10^{-4}$ rads (Jiang et al., 2013b). The cross-correlation based EBSD technique is often referred as high resolution EBSD (HR-EBSD). The detailed descriptions and mathematical frameworks for this method can be found in a number of publications (Arsenlis and Parks, 1999; Britton and Wilkinson, 2011, 2012; Pantleon, 2008; Wilkinson and Randman, 2010a; Wilkinson et al., 2006a) and will not be repeated in detail here.

Briefly the stored GND content results in lattice curvature, some components of which can be determined from EBSD patterns captured in a map across a grain. Within each grain, a reference pattern was selected that had relatively high image quality and came from a point well away from any grain boundary. All other test patterns within that grain were compared to this reference pattern. The X and Y shifts of features within the diffraction pattern between reference and test patterns were determined at 50 sub-regions dispersed across the pattern using image cross-correlation method. Assuming the free surface is traction free; all 9 components in the deformation gradient tensor can be obtained. This allows the elastic strain and lattice rotation to be determined respectively by splitting the symmetric and asymmetric terms from the deformation gradient matrix (using an infinitesimal decomposition, though other methods may be used (Benjamin Britton and Wilkinson, 2012)). As the contribution of elastic strain gradients to the GND measurement is found to be significantly smaller than the rotation gradients, it was neglected in the analysis (Wilkinson and Randman, 2010b). The EBSD technique can only probe variation with position within the free surface (two dimensional) and information along the third direction normal to the free surface is not usually accessible. This provides six constraints corresponding to five of nine Nye's tensor components and one difference (Pantleon, 2008; Wilkinson and Randman, 2010b). In FCC crystalline materials, there are 12 possible slip systems which contain 12 pure edge and 6 pure screw dislocations types in {111} slip planes and <110> slip directions. This therefore provides an underdetermined problem, with fewer constraints than potential dislocation types for which we want to determine densities. There are many routes discussed in the literature to treat this problem (Britton et al., 2009; Gardner et al., 2010; Kysar et al., 2010; Kysar et al., 2007; Sun et al., 2000) (Arsenlis and Parks, 1999; Field et al., 2010; Hardin et al., 2011; Hardin et al., 2013; Ruggles and Fullwood, 2013) (Demir et al., 2009), with varying degrees of success and merit. We choose to select a solution that physically supports the curvature measured and also minimises the total line energy, accounting for differences between screw and edges using isotropic elastic energies, of the dislocations used (this a L^1 minimisation scheme). For numerical stability when applying our minimisation scheme in Matlab, both positive and negative slip directions are taken into account separately, but all densities are constrained to be positive. A full description of the GND density formulation is given in the appendix.

1.3 Taylor factor

The Taylor factor ***M*** is a geometric factor used in analysis of plastic deformation in polycrystals to describe the relative amount of work required to deform grains to the same strain in order to satisfy the compatibility condition (Taylor, 1934). Taylor assumed that multiple slip systems are activated in all grains so that they can deform to the same uniform macroscopic plastic strain. Equilibrium condition is however ignored in the theory.

In Taylor's theory, it is assumed that the critical resolved shear stress on all the activated slip systems is the same. Additionally according to Von Mises criteria, at least five slip systems are required to accommodate an arbitrarily shape change. Therefore the Taylor approach requires five or more slip systems to be active and then Taylor calculated the energy expenditure for all possible

sets of slip systems, and the Taylor factor is related to the minimum energy solution from all the possible permutations of different active slip systems. It is very computational expensive to work out the correct set of slip systems for this minimum energy problem. For instance in FCC crystals, there are 792 sets of possible combination to choose 5 slip systems. Taylor later showed the number of combinations can be reduced to 96 as many of the 792 combinations cannot produce 5 independent strains (Taylor, 1934).

A slightly simpler, but related route was proposed by Bishop and Hill (Bishop and Hill, 1951a; Bishop and Hill, 1951b) which we follow here. We identify all the stress states to simultaneously activate five or more slip systems. This results in only 28 different stress states that activate five or more slip systems while not exceeding this stress on any of the remaining systems. From this route, similar to Taylor's approach of finding the minimum energy, Bishop and Hill determine which one of these 28 stress states is the most appropriate to produce the given strain state from the principle of maximum virtual work.

In this paper, the Taylor factor was determined in a Matlab script by employing Bishop and Hill's method. Firstly three Euler angles $(\varphi_1, \varphi_2$ and $\emptyset)$ were converted into orientation matrix **g** according to Eq.(1), using Bunge's convention and the sample coordinate systems are defined as shown in Figure 1, with the X axis pointing along the Rolling Direction (the OIM convention).

$$g_{ij} = \begin{pmatrix} cos\varphi_1 cos\varphi_2 - sin\varphi_1 sin\varphi_2 cos\emptyset & sin\varphi_1 cos\varphi_2 + cos\varphi_1 sin\varphi_2 cos\emptyset & sin\varphi_2 sin\emptyset \\ -cos\varphi_1 sin\varphi_2 - sin\varphi_1 cos\varphi_2 cos\emptyset & -sin\varphi_1 sin\varphi_2 + cos\varphi_1 cos\varphi_2 cos\emptyset & cos\varphi_2 sin\emptyset \\ sin\varphi_1 sin\emptyset & -cos\varphi_1 sin\emptyset & cos\emptyset \end{pmatrix} \quad \textbf{Eq.(1)}$$

For the uniaxial deformation of copper utilised in this paper, the unity von Mises strain $\varepsilon_{ij}^{sample}$ in sample coordinate can be defined as $\begin{pmatrix} 1 & 0 & 0 \\ 0 & -0.5 & 0 \\ 0 & 0 & -0.5 \end{pmatrix}$. The sample coordinate strain was transformed to crystal coordinate by Eq.(2).

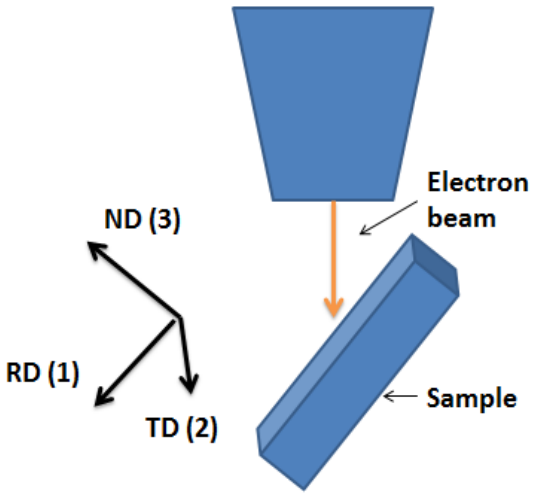

Figure 1, the three principle reference axes in OIM analysis software.

$$\varepsilon_{ij}^{crystal} = g_{ij}\,\varepsilon_{ij}^{sample}\,g_{ij}^{T} \qquad \textbf{Eq.(2)}$$

Since the strain state on crystal was obtained, the work increment for each of the 28 stress states can thus be calculated by Eq.(3). Values of A, B, C, F, G and H are described in Table 1 (Hosford, 1993).

$$dW = \sqrt{6}\tau\,(-Bd\varepsilon_{11}^{crysal} + Ad\varepsilon_{22}^{crysal} + 2Fd\varepsilon_{23}^{crysal} + 2Gd\varepsilon_{13}^{crysal} + 2Hd\varepsilon_{12}^{crysal}) \qquad \textbf{Eq.(3)}$$

The virtual work increment, dW, can be calculated using Eq.(3), where τ is the critical resolved shear stress that is a constant for all slip systems and

$$A = \frac{\sigma_{22}-\sigma_{33}}{\sqrt{6}\tau},\ B = \frac{\sigma_{33}-\sigma_{11}}{\sqrt{6}\tau}, C = \frac{\sigma_{11}-\sigma_{22}}{\sqrt{6}\tau}, F = \frac{\sigma_{23}}{\sqrt{6}\tau}, G = \frac{\sigma_{31}}{\sqrt{6}\tau}\ and\ H = \frac{\sigma_{12}}{\sqrt{6}\tau}$$

For each orientation, the appropriate stress state is the one with maximum work increment ***dW.***

The Taylor factor is defined as the maximum work increment divided by the von Mises equivalent strain and critical resolved shear stress:

$$M = \frac{dW_{max}}{\tau d\varepsilon_{vM}} \qquad \textbf{Eq.(4)}$$

Since the applied von Mises equivalent strain ($\boldsymbol{\varepsilon_{vM}}$) is a unity, substituting Eq.(3) into Eq.(4) we can calculate Taylor factor using Eq.(5):

$$M = \frac{dW_{max}}{\tau d\varepsilon_{vM}} = \sqrt{6}\,(-Bd\varepsilon_{11}^{crysal} + Ad\varepsilon_{22}^{crysal} + 2Fd\varepsilon_{23}^{crysal} + 2Gd\varepsilon_{13}^{crysal} + 2Hd\varepsilon_{12}^{crysal}) \qquad \textbf{Eq.(5)}$$

	A	B	C	F	G	H
1	1	-1	0	0	0	0
2	0	1	-1	0	0	0
3	-1	0	1	0	0	0
4	0	0	0	1	0	0
5	0	0	0	0	1	0
6	0	0	0	0	0	1
7	0.5	-1	0.5	0	0.5	0
8	0.5	-1	0.5	0	-0.5	0
9	-1	0.5	0.5	0.5	0	0
10	-1	0.5	0.5	-0.5	0	0
11	0.5	0.5	-1	0	0	0.5
12	0.5	0.5	-1	0	0	-0.5
13	0.5	0	-0.5	0.5	0	0.5
14	0.5	0	-0.5	-0.5	0	0.5

	A	B	C	F	G	H
15	0.5	0	-0.5	0.5	0	-0.5
16	0.5	0	-0.5	-0.5	0	-0.5
17	0	-0.5	0.5	0	0.5	0.5
18	0	-0.5	0.5	0	-0.5	0.5
19	0	-0.5	0.5	0	0.5	-0.5
20	0	-0.5	0.5	0	-0.5	-0.5
21	-0.5	0.5	0	0.5	0.5	0
22	-0.5	0.5	0	-0.5	0.5	0
23	-0.5	0.5	0	0.5	-0.5	0
24	-0.5	0.5	0	-0.5	-0.5	0
25	0	0	0	0.5	0.5	-0.5
26	0	0	0	0.5	-0.5	0.5
27	0	0	0	-0.5	0.5	0.5
28	0	0	0	0.5	0.5	0.5

Table 1, Bishop and Hill stress states for FCC crystals (Bishop and Hill, 1951b)

1.4 Analysing Proximity to Grain Boundaries

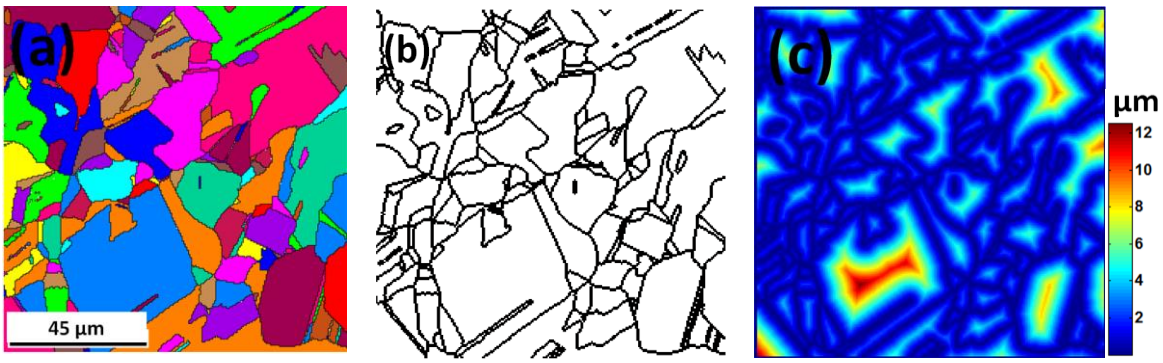

Figure 2, demonstration maps grain boundary and Euclidian distance calculations, using a map from Cu deformed to 10% strain, mapped over 112µmx112µm, 0.5 µm step size (a) grain coloured map (b) binary grain boundary map. (c) Calculated shortest Euclidean distance to the nearest surface grain boundary.

Here we aim to analyse the GND density data in terms of proximity to grain boundaries as well as with respect to the Taylor factor for a given grain. An EBSD map of the sample deformed to 10% uniaxial strain will be used here and in the following subsections to demonstrate how data was processed in Matlab. The OIM grain identification (GID) map was generated using a threshold with misorientation of 10 degrees and was imported into Matlab as shown in Figure 2 (a). Grain boundaries were identified using a 3x3 kernel to identify boundary points (the detailed process is illustrated in Figure 3) and produced a binary grain boundary map, as shown in Figure 2 (b). Note that points along the edges of EBSD map were excluded from this calculation.

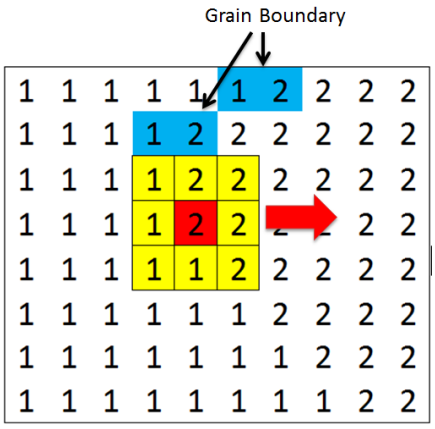

Figure 3, a schematic diagram to show grain boundary identification process. The digital number corresponds to grain IDs and the blue colour cells are identified grain boundary points. The 3x3 kernel box is running from the top of Grain ID map to determine the locations of GBs by comparing the central point with its eight neighbouring points. If different Grain ID number present between the central point and any of the eight neighbouring points, the central point is identified as a GB points. The calculated binary GB map is shown in Figure 2 (b).

The Euclidean distance of the test point to all the points on the grain boundaries were calculated and the one with minimum magnitude was identified as the Euclidean distance to the nearest grain boundary, as is expressed in Eq.(6).

$$Minimum\ (Euclidean\ distance\ (i,j)) = \sqrt{(X_i - X_{GB})^2 + (Y_i - Y_{GB})^2} \quad \textbf{Eq.(6)}$$

Where X_i and Y_i are the coordinates of the testing point, while X_{GB} and X_{GB} correspond to the coordinates of all grain boundary points. The calculated minimum Euclidean distance to grain boundaries for the example data set is shown in Figure 2 (c).

This step has been explained explicitly as determination of Euclidean distance to the nearest grain boundary is critical as it is used to filter the data points (Taylor factor (as shown in Figure 4(a)) and GND density (as shown in Figure 4 (b)) with respect to the distance to grain boundaries. This builds on prior work by the Authors (Jiang et al., 2013a; Jiang et al., 2012) where it was found that in moderately and severely deformed polycrystalline copper samples, the GND density at distances up to ~1.5µm from grain boundaries showed a marked contrast to those nearer the grain interior. This 1.5µm distance has been selected as a threshold within this work to define a 'mantle' zone adjacent to grain boundaries. The points that have larger distance to grain boundaries were defined as belong to 'grain interior' or 'core' zone. This separation process is illustrated in Figure 4.

	Taylor Factor	GND Density
All Probed Points	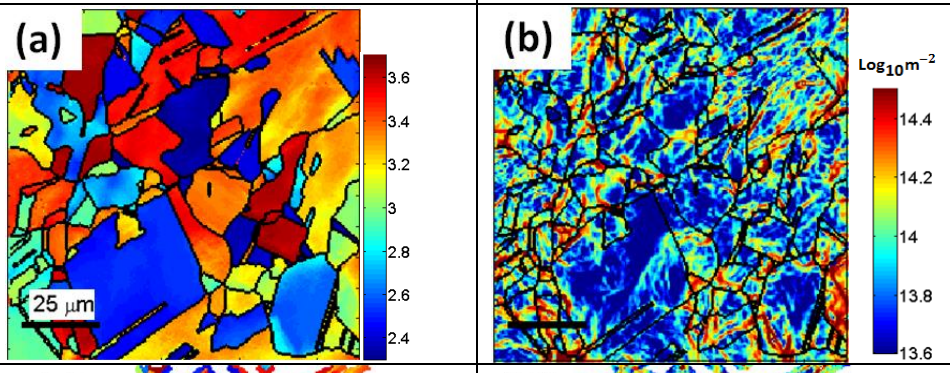	
Grain Mantle Zone	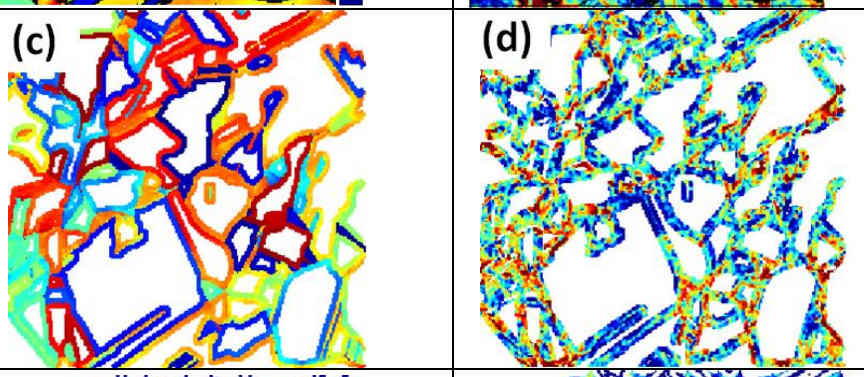	
Grain Core Zone	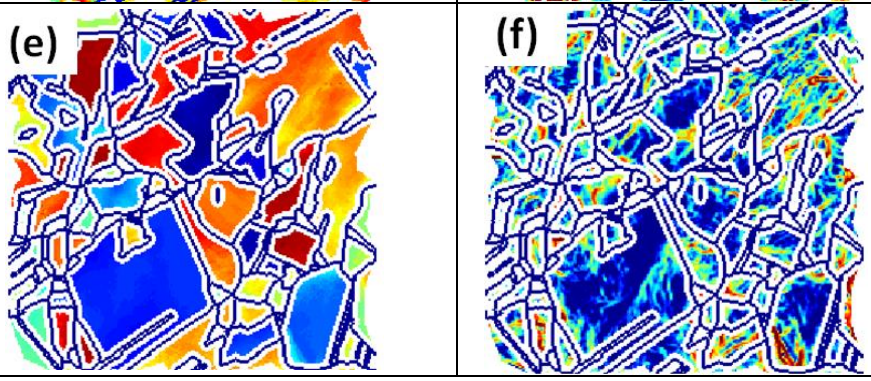	

Figure 4 showing Taylor factor (a, c, e) and GND density maps (b, d, f) of the 10% strained copper sample, the loading axis is along the vertical direction (RD). Grain boundaries are defined with a misorientation tolerance of 10°. Probed points with minimum Euclidean distance to the edges of map less than the distance to grain boundaries are excluded. (a) Taylor factor map of all probed points (b) GND density map of all probed points; (c) Taylor factor map of grain mantle zone (Euclidean distance < 1.5μm);; (d) GND density map of grain mantle zone; (e) Taylor factor map of grain core zone (Euclidean distance > 1.5μm); (f) GND density map of grain core zone.

3. Results

1.5 The dislocation structures and their evolution

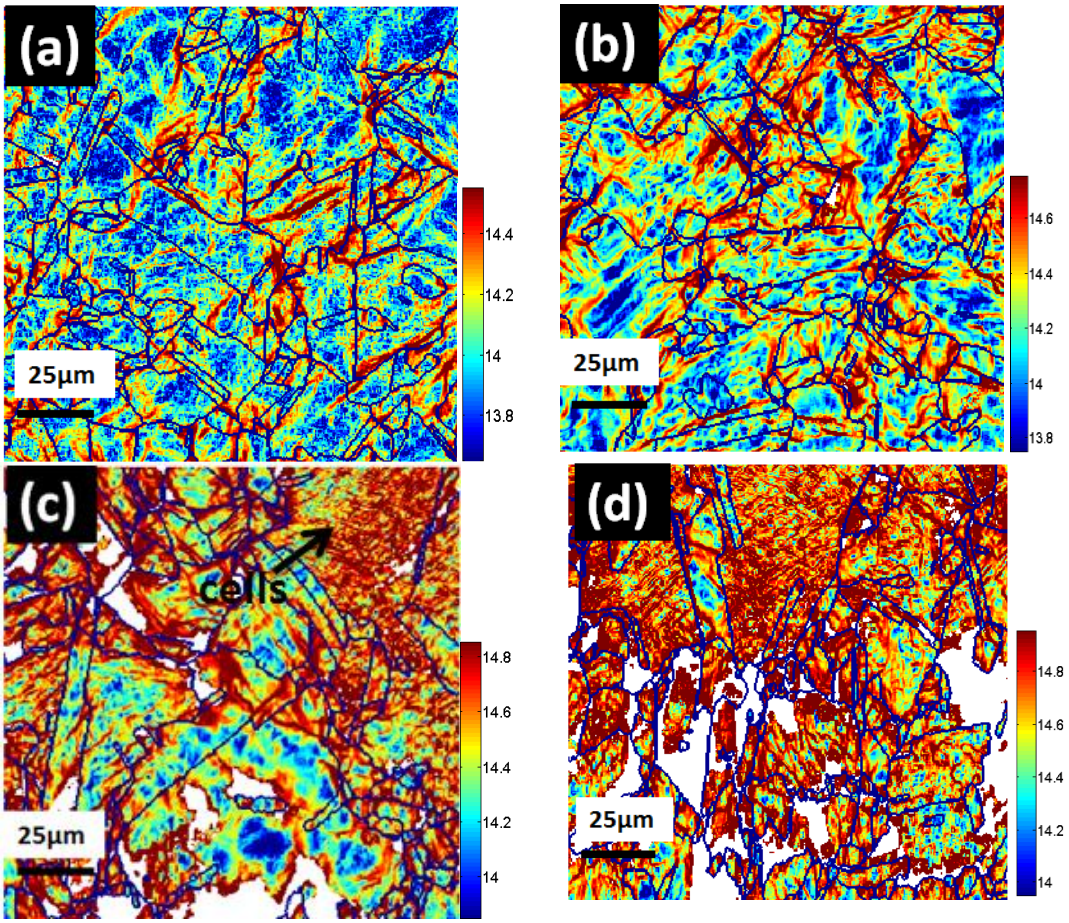

Figure 5, 150μm x150μm GND density maps extracted from the central regions of the 500μm x500μm GND maps in copper samples (Jiang et al., 2013a) which were deformed under tensile strains at 6% (a), 10% (b), 25.5%(c) and 40%(d). The colour scales were in $\log_{10}$ scale and were adjusted for individual map to highlight dislocation structures. Dark blue lines represent GBs with minimum misorientation angle of 10 degrees between neighbouring pixels. The white areas showing in (c) and (d) consist of rejected points from reliability assessment in cross-correlation analysis. The loading axis is along the vertical direction of the maps (RD).

Significantly heterogeneous deformation structures were developed during plastic deformation. At 6% strain, as shown in Figure 5(a), dislocation cells are observed in some grains. The GND density stored in dislocation cell walls is estimated as $2x10^{14}$ m^{-2} while in dislocation cell interiors the GND density is estimated as $0.2x10^{14}$ m^{-2} though there is considerable variation across the map. The most pronounced features in this map are curved band-liked structures with relatively high GND densities stored within them (dislocation bands). Most of these bands are oriented in a range between 35-55 degrees to the loading axis (vertical). Some of them are formed within grains and others span across grains and grain boundaries and therefore form a connected dislocation network covering multiple grains. The morphologies of these bands vary in different grains e.g. wavy, curved and straight bands.

In the 10% strained sample (see Figure 5(b)) a higher fraction of dislocation bands were formed. Comparing to 6% strained map, the bands have evolved into a thicker forms with higher GND densities and have more branches.

Various grain orientations have developed different dislocation structure. In some grains, straight dislocation bands are perpendicular to each other. In some grains dislocation cells are well defined, and relatively uniformly distributed. In other grains subdivision takes place such that grains are divided into a few domains by dislocation bands. The paths of some main dislocation bands follow along some grain boundaries.

At higher deformation levels (25.5% and 40%) clear dislocation cell arrays are displayed e.g. at the top right corner in Figure 5(c). Comparing with the former maps (6% and 10%), the dislocation cell arrays evolved into more compact arrangements. Long range dislocation bands are absent. In other grains the dislocation density difference between dislocation cell interiors (~8×10^{13} m^{-2}) and dislocation cell boundaries (~2.5×10^{15} m^{-2}) are extremely large. Despite the areas (in white) where cross-correlation data fell below data quality threshold, dislocation networks are still well defined. Further development of grain subdivision can also be observed.

In the final map (40%) as shown in Figure 5(d), the spatial distribution of cell arrays and separation of cell walls is very consistent within some grains of particular orientations (which is discussed in more detail later). Furthermore long range dislocation band networks are not as clearly observed.

Areas of the maps where data quality threshold were not met were assessed. The pattern quality of many of patterns within these regions was individually checked and Kikuchi bands were clearly present. Failure to meet the thresholds was due to a significant difference between the crystal orientation of the reference point within the grain and the measurement point, which results in a lack of consistent features to be successfully cross-correlated. Hence the white areas do not give a large bias to the statistics.

1.6 The orientation dependence of dislocation structure development

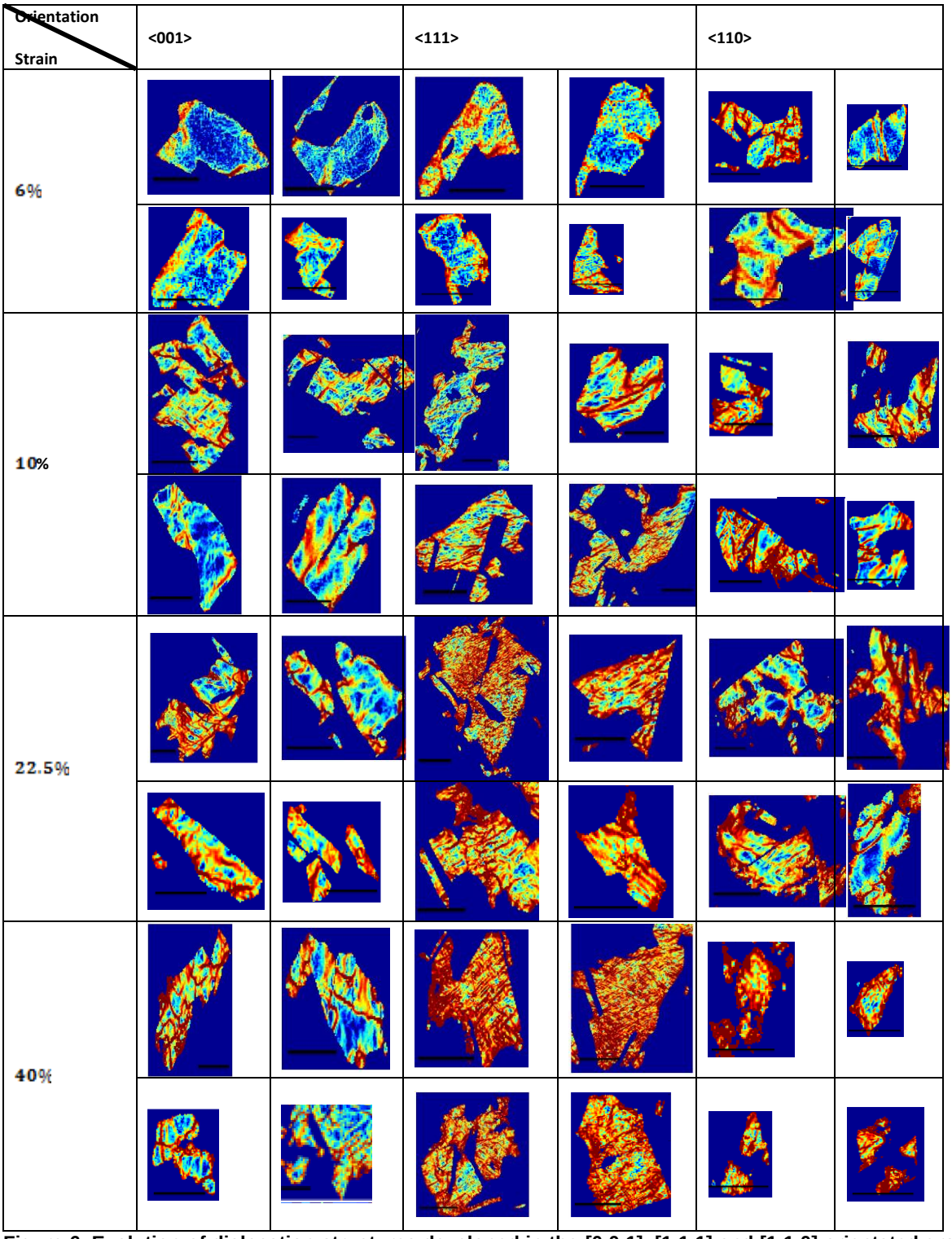

Figure 6, Evolution of dislocation structures developed in the [0 0 1], [1 1 1] and [1 1 0] orientated grains selected from the four large 500μm x500 μm GND density maps. Colour scales for each strain state are different and optimised as Figure 5 to highlight changes in dislocation structure morphology. The displayed scale bar is 20 μm.

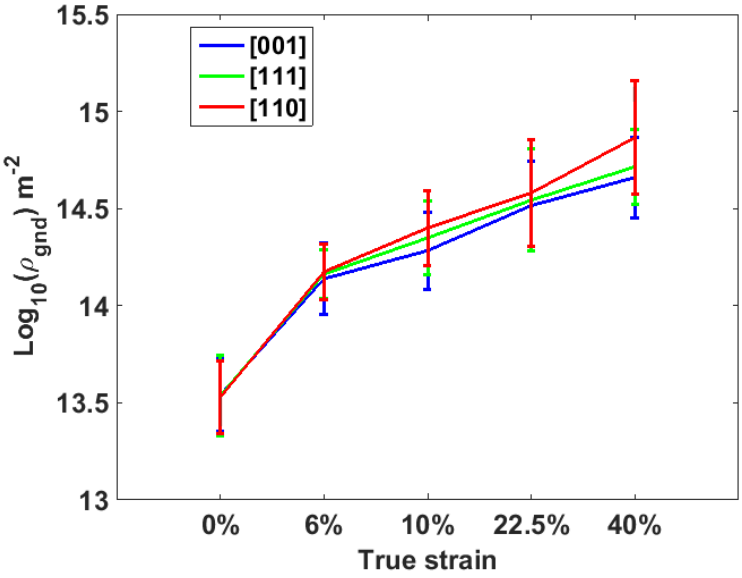

Figure 7, grain averaged GND density with three different grain orientation plot as a function of imposed plastic strain. The error bars indicate standard deviation of grain averaged GND density in a particular orientation.

As seen in the preceding subsection, distinct dislocation patterns had been formed in some grain orientations at each of the four deformation levels. In this subsection, four grains were selected for each of the three orientations <001>, <111> and <110> from each of the GND density maps. The GND density patterns for these grains are shown in Figure 6. This allows direct qualitative visual assessment of dislocation structures.

At moderate strains (6% and 10%), both dislocation bands and cell array structure can be found in all three selected orientations. Dislocation bands are arranged in rather wavy forms in all grains. With further deformation, it is of interest to note that grains with different orientations exhibit distinct dislocation structures. In<111> orientated grains more homogenous, linear and dense dislocation cell arrays are formed and fewer dislocation bands are present. However the dislocation bands which divide grains into several domains are common features found in <110> grains. Both dislocation cells and dislocation boundaries are presented in <001> grains.

These orientation dependent tendencies seem to become more obvious with increasing strains. More homogenous cell array structures in <111> orientated grains are developed at 40% strain. The size of dislocation cells formed mainly in <001> grains is reduced and better defined dislocation band networks are formed within the grains. The <110> grains show relatively higher grain average dislocation density comparing to <111> and <001> ones and in <110> grains GBs become the preferential sites for dislocation accumulation.

Due to grain rotation with increasing plastic deformation, the number of <110> grains becomes smaller and few large grains of <110> orientation was present in 40%. Hence those selected <110> grains are smaller than <111> and <001> grains.

Quantitative analysis of grain averaged GND density behaviour on these three orientations was carried out and shown in Figure 7. Clearly the <110> oriented grains have on average stored higher

GND density compared to <001> and <111> orientation grains. Furthermore this tendency becomes more obvious with increasing strain. Although the average behaviour shows grain orientation dependence there is considerable overlap in the range of GND densities found within each group of grains. This suggests that grain size and neighbouring grain orientations also have significant influence on the GND density within any particular grain.

1.7 Correlation between Taylor factor and GND density

1.7.1 Whole map analysis of Taylor factor and GND density

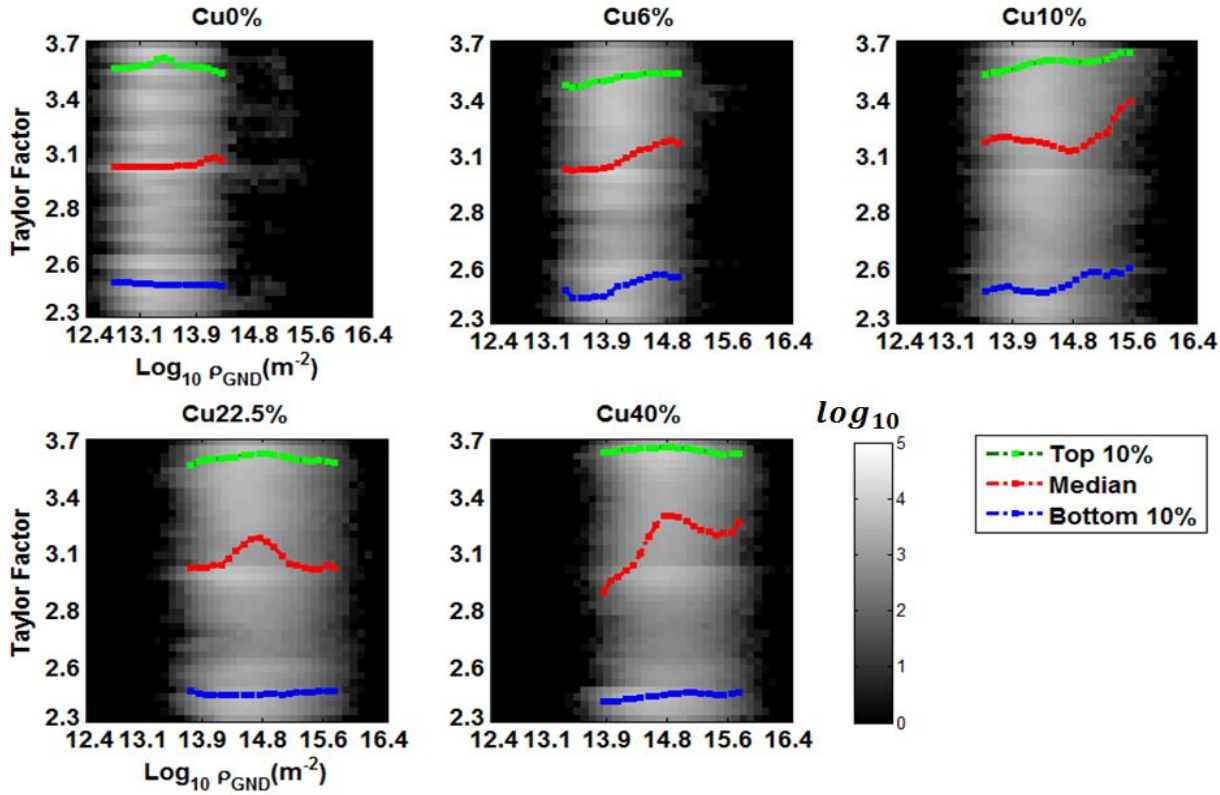

Figure 8, the analysis of Taylor factor correlations with GND density for all probed points in the 0%, 6%, 10%, 22.5% and 40% tensile strained polycrystalline copper maps. The determined GND density and Taylor factor data was binned into 40 bins along both x and y axes. For the each vertical bin, similar to histogram vertical bar, the 10%, 50% and 90% percentiles points were found and plotted with green, red and blue colours. The 10%, 50% and 90% points were joined up for all 40 vertical bins to describe the general trend of the correlation. To minimise the sampling problem, minimum 1200 probed points for each vertical bin were required to calculate the three percentiles. The black and white background intensity at $\log_{10}$ scale represents the number of sampled points in each bin.

Since data from a large number grains (~1600s) has been acquired and processed in each map, this allows quantitative analysis to be carried out. Statistical analysis on the correlation and evolution between Taylor factor and GND density were conducted on all copper sample maps. Due to the large number of data points (1 million points per map); a unique figure was designed to investigate the relation between the Taylor factor and GND density as shown in Figure 8.

It is found that in the annealed sample (Figure 8, Cu0%), GNDs do not seem to have any preferential grains to accumulate in. The high GND density end and low GND density end are almost equally distributed in all grains orientation and hence Taylor factor. Therefore the top 10%, median and bottom 10% lines are found to be approximately flat. Tensile axis is assumed to be along RD even

though no deformation was actually imposed on it. The flat lines imply that there is no texture (formed after annealing process) influence on the initial GND density distribution. However in the 6% strained specimen the high GND density showed a marked dependence on the Taylor factor. The three percentile lines show that the higher GND density points ('hot' spots) prefer to assemble in the points with the larger Taylor factor magnitude ('hard' grains). As the plastic deformation increases, the general correlation between the high GND density and large Taylor factor becomes stronger, though a small fluctuation occurs in the lower GND density end. The increasing gradient in the median percentile curve shows that more points with high GND density were found in the 'hard' grains.

In the 22.5% strained sample, the GND density hot spots no longer appear in hard grains (Figure 8). Although the median line increases from the low GND density side to reach a peak around the middle range of GND density, it subsequently drops and becomes flat at the high GND density end. This reduction in median Taylor factor associated with higher GND density is anomalous compared to the other deformation states examined.

The strongest gradient of the median percentile line is found in 40% strained sample at the lower GND density range. Similar to the 22.5% strained sample, the gradient becomes slightly negative after passing the middle point.

1.7.2 Taylor factor and GND density analysis near grain boundaries (GBs)

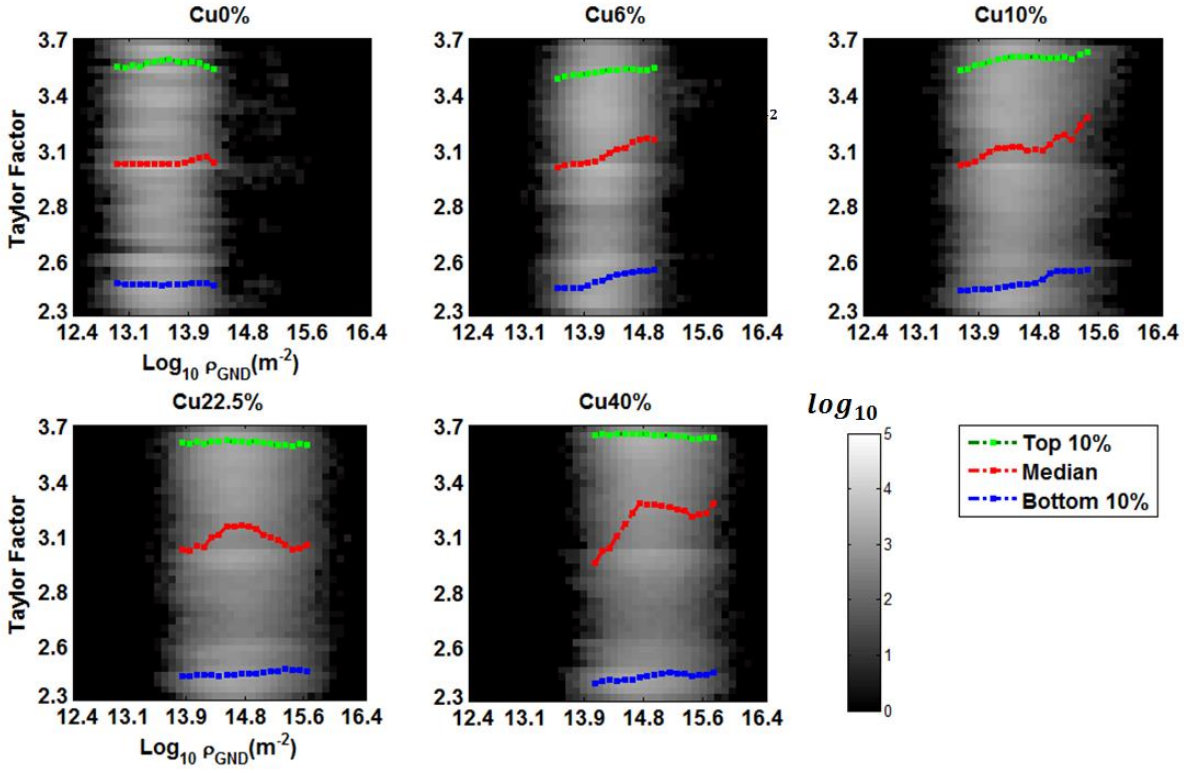

Figure 9, point to point based Taylor factor and GND density analysis focusing on the points adjacent to grain boundaries. The same type of figure is constructed as Figure 8 however only points with the minimum Euclidean distance less than 1.5 μm to grain boundaries are included in these plots. ~35% of each map is included in these near GB datasets.

Comparing to the previous analysis for all points in a map, similar trends are found for the probed points near grain boundaries. The points with high GND density tend to have larger magnitude of

Taylor factor and this correlation becomes stronger with the increasing deformation. Although, there is still a breakdown in the middle of the 22.5% and 40% datasets for the relatively high GND density points, the gradient in the first part of the median point curves shows increasing strength in the correlation between the GND density and Taylor factor. Furthermore, the relation seems smoother and clearer comparing to Figure 8 especially in the 10% strained sample.

4. Discussion

The cross-correlation based HR-EBSD approach has been employed to measure the geometrically necessary dislocation density in OFHC copper polycrystals deformed under progressive uniaxial tension (0%, 6%, 10%, 22.5% and 40% strains). Statistically large datasets were collected with 1 million probed points and ~1600 grains included at each strain state.

Previous characteristic dislocation structures reported from TEM studies of deformed polycrystalline copper (Gottler, 1973; Huang and Winther, 2007) such as dislocation cells, dislocation bands, 'herring bone' dislocation network have also been observed in the HR-EBSD derived GND density maps as shown in Figure 5 (a), (b), (c) and (d). This shows that our HR-EBSD GND density measurement complement prior work. However comparing to TEM observation, instead of focusing on the dislocation structures in one or two grains, GND density maps reveal information at larger scale especially for those dislocation bands spanning across several grains and the complicated dislocation networked developed in the more highly deformed sample. These new experimental results should prove valuable to the modelling community in validating advanced simulations aimed at capturing grain and sub-grain patterning of plastic strain accommodation along with the role of compatibility and GND density distributions on local stresses and overall hardening during plastic deformation of polycrystals.

These dislocation networks suggest that the formation of dislocation bands are not merely constrained within one or two grains but are developed and connected in a large number of grains. This connected dislocation network allows all grains to work as one unit to accommodate the imposed plastic deformation. Such features developing over many neighbouring grains are not well captured by conventional methods such as TEM or X-ray and neutron diffraction. However, DIC observations (Carroll et al., 2013; Littlewood and Wilkinson, 2012b) and the resulting longer length scale patterning of dislocation density revealed here by HR-EBSD suggest that the sphere of influence of a particular grain on the overall pattern of deformation may extend a considerable distance. This may have significant implications for the volumes of material that must be simulated to avoid the deformation patterns being dominated by the boundary conditions imposed on the system.

The dislocation structure evolution with progressive straining is also of great interest to understand the mechanisms of the dislocation networks. At the lightly strained sample (2% and 6%), grain subdivision by dislocation boundaries are commonly shown in most of the grains regardless of their orientations. This indicates that in the early stage of plastic deformation, the formation of dislocation structures are strongly influenced by grain-grain interactions. The accumulation of high GND density and terminal morphology formed near triple junctions implies the strong neighbouring grains effects. Triple junctions serving as preferential dislocation accumulation sites have been quantitatively studied and proved by the authors in a previous publication (Jiang et al., 2013a).

As the imposed plastic deformation increases, together with the grain rotation (texture development: grains rotate toward <111> orientation) more and more grains have well defined regular dislocation cells. The phenomenon has been qualitatively examined in Figure 6. In the heavily deformed samples,

dislocations in the grains with <111> orientation are commonly found to form dislocation cells structure while dislocation bands are often found in the <001> and <110> oriented grains. It seems the initial heterogeneous deformation structures evolve toward to a rather more homogenous pattern. This probably is a more efficient arrangement such that the plastic deformation can be more evenly accommodated. However, due to the large number of possible slip systems, FCC crystals in general are so ductile that allows this transformation to occur. This may not be possible for other materials with fewer slip options such as the HCP metals.

It should be noted that the HR-EBSD GND density approach depends on the size of the user defined Burgers circuit and only recovers the dislocation density causing lattice curvature over the length scale set by the size of the Burgers circuit. The effects and sensitivity has been studied by the authors in the previous publication (Jiang et al., 2013b). The 0.5μm step size used in this study cannot separate dislocations present in dipoles or multi-poles with separations smaller than the step size. The dislocation structure of these statistically stored dislocations cannot be recovered using the HR-EBSD technique.

The data collection was designed so that a relatively large number of grains were mapped at each strain state so as to enable statistical analysis of the results. The Taylor factor was used in this study as an indicator to quantify how 'hard' or 'soft' grains are but it should be noted that the assumption of homogenous strain and disregard for force equilibrium implicit in such a simplified analysis is a significant limitation. Figure 8 and Figure 9 show analysis of the correlation between GND density and Taylor factor based on either the whole maps (Figure 8) or limited to points near grain boundaries (Figure 9) has been presented. The results suggest that in general the high GND density points/grains have a tendency to be stored in 'hard' grains (high Taylor factor) and this tendency becomes stronger with progressively larger strain. The high Taylor factor grains require larger stress to achieve the imposed uniform geometrical change (Taylor theory (Taylor, 1934)), and thus more work is expended in their deformation and is stored as a higher dislocation density. Therefore, points with high GND density are found in the grains with high Taylor factor. Points adjacent to the grain boundaries also showed this correlation which suggests that GNDs may be stored near grain boundaries within the high Taylor factor grains as part of the local accommodation of grain-grain incompatibility interactions.

The orientation dependence shown in figure 7 is in a good agreement with GND measurement using conventional EBSD approach in pure aluminium sample deformed in channel die compression by Merriman et al (Merriman et al., 2008). They also found that orientation with higher Taylor factor stored more GNDs than the lower ones. However, in their study only three orientations <001> <111> and <110> orientations were investigated and the only moderate plastic deformation states rather than a wide range of plastic deformation states were mapped (5%, 10% and 15% strain under compression). Similar findings have also been reported using X-ray line broadening (Kallend and Huang, 1984) .

It should be pointed out that as the data was collected from four different samples and the original microstructure for each deformed sample was unknown, it is difficult to distinguish whether the high Taylor factor grains were 'hard' prior to the plastic deformation or they are the results of grain orientation rotation (texture).

5. Conclusion

Characteristic dislocation arrangements were observed in the GND density maps similar to those found using the TEM techniques, such as dislocation cells, dislocation bands and dislocation networks. The HR-EBSD technique for quantitative and detailed characterisation of deformation structures over relatively large areas has been demonstrated as a very valuable asset for studying plastic deformation process in polycrystalline materials.

It showed that in polycrystalline materials, grains tend to deform together and rather complicated dislocation networks connected across a large number of grains were developed during the plastic deformation process. This implied that grain-grain interaction play important role in dislocation network formation.

The formation of dislocation bands and cells in grains with distinctive orientations demonstrated that dislocation network development has strong orientation dependence. Some grains such as grains with <110> and <001> appear more easily influenced by neighbouring grains than others (grains with <111> orientation).

High GND density points are found to appear in grains of high Taylor factor ('hard' grains) both within the grain interior and in the regions close to the grain boundaries. Although more work is needed, this analysis suggests that strain difference between neighbouring grains may be accommodated in the high Taylor factor 'hard' grains rather than low Taylor factor 'soft' grains.

Acknowledgements

The authors are very grateful for the insightful and inspiring discussion with Prof A. Rollet.

References

Abuzaid, W.Z., Sangid, M.D., Carroll, J.D., Sehitoglu, H., Lambros, J., 2012. Slip transfer and plastic strain accumulation across grain boundaries in Hastelloy X. Journal of the Mechanics and Physics of Solids 60, 1201-1220.

Adams, B.L., Kacher, J., 2010. EBSD-based microscopy: Resolution of dislocation density. Computers, Materials, & Continua 14, 185-196.

Allain-Bonasso, N., Wagner, F., Berbenni, S., Field, D.P., 2012. A study of the heterogeneity of plastic deformation in IF steel by EBSD. Materials Science and Engineering: A 548, 56-63.

Als-Nielsen, J., McMorrow, D., 2011. Elements of modern X-ray physics. John Wiley & Sons.

Arsenlis, A., Parks, D., 1999. Crystallographic aspects of geometrically-necessary and statistically-stored dislocation density. Acta Materialia 47, 1597-1611.

Britton, T., Wilkinson, A.J., 2012. Stress fields and geometrically necessary dislocation density distributions near the head of a blocked slip band. Acta Materialia 60, 5573-5582.

Bishop, J., Hill, R., 1951a. CXXVIII. A theoretical derivation of the plastic properties of a polycrystalline face-centred metal. Philosophical Magazine Series 7 42, 1298-1307.

Bishop, J., Hill, R., 1951b. XLVI. A theory of the plastic distortion of a polycrystalline aggregate under combined stresses. Philosophical magazine 42, 414-427.

Britton, T., Wilkinson, A., 2011. Measurement of residual elastic strain and lattice rotations with high resolution electron backscatter diffraction. Ultramicroscopy 111, 1395-1404.

Britton, T., Wilkinson, A., 2012. High resolution electron backscatter diffraction measurements of elastic strain variations in the presence of larger lattice rotations. Ultramicroscopy 114, 82-95.

Britton, T., Liang, H., Dunne, F.P.E., Wilkinson, A.J., 2009. The effect of crystal orientation on the indentation response of commercially pure titanium: experiments and simulations. Proceedings of the Royal Society A: Mathematical, Physical and Engineering Sciences 466, 695-719.

Carroll, J.D., Abuzaid, W., Lambros, J., Sehitoglu, H., 2013. High resolution digital image correlation measurements of strain accumulation in fatigue crack growth. International Journal of Fatigue 57, 140-150.

Chekhonin, P., Engelmann, J., Oertel, C.G., Holzapfel, B., Skrotzki, W., 2014. Relative angular precision in electron backscatter diffraction: A comparison between cross correlation and Hough transform based analysis. Crystal Research and Technology 49, 435-439.

Demir, E., Raabe, D., Zaafarani, N., Zaefferer, S., 2009. Investigation of the indentation size effect through the measurement of the geometrically necessary dislocations beneath small indents of different depths using EBSD tomography. Acta Materialia 57, 559-569.

Field, D., Magid, K., Mastorakos, I., Florando, J., Lassila, D., Morris Jr, J., 2010. Mesoscale strain measurement in deformed crystals: A comparison of X-ray microdiffraction with electron backscatter diffraction. Philosophical Magazine 90, 1451-1464.

Field, D., Merriman, C., Allain-Bonasso, N., Wagner, F., 2012. Quantification of dislocation structure heterogeneity in deformed polycrystals by EBSD. Modelling and Simulation in Materials Science and Engineering 20, 024007.

Fultz, B., Howe, J., 2012. Transmission electron microscopy and diffractometry of materials. Springer.

Gardner, C.J., Adams, B.L., Basinger, J., Fullwood, D.T., 2010. EBSD-based continuum dislocation microscopy. International Journal of Plasticity 26, 1234-1247.

Gottler, E., 1973. Dislocation arrangement and work-hardening of copper single crystals with [100] axis orientation. I. Dislocation arrangement and cell structure of crystals deformed in tension. Phil. Mag 28, 1057-1076.

Guinier, A., 2013. X-ray diffraction: in crystals, imperfect crystals, and amorphous bodies. Courier Dover Publications.

Hardin, T., Adams, B.L., Fullwood, D.T., Wagoner, R.H., 2011. Estimation of the Full Nye Tensor by EBSD-Based Dislocation Microscopy, Materials Science Forum, p. 489.

Hardin, T.J., Adams, B.L., Fullwood, D.T., Wagoner, R.H., Homer, E.R., 2013. Estimation of the full Nye's tensor and its gradients by micro-mechanical stereo-inference using EBSD dislocation microscopy. International journal of plasticity 50, 146-157.
Hosford, W.F., 1993. The mechanics of crystals and textured polycrystals. Oxford University Press(USA), 1993, 248.
Huang, X., Winther, G., 2007. Dislocation structures. Part I. Grain orientation dependence. Philosophical Magazine 87, 5189-5214.
Ice, G.E., Larson, B.C., Yang, W., Budai, J.D., Tischler, J.Z., Pang, J., Barabash, R., Liu, W., 2005. Polychromatic X-ray microdiffraction studies of mesoscale structure and dynamics. Journal of synchrotron radiation 12, 155-162.
Jackson, M.A., Groeber, M.A., Uchic, M.D., Rowenhorst, D.J., De Graef, M., 2014. h5ebsd: an archival data format for electron back-scatter diffraction data sets. Integrating Materials and Manufacturing Innovation 3, 1-12.
Jiang, J., Britton, T., Wilkinson, A., 2013a. Evolution of dislocation density distributions in copper during tensile deformation. Acta Materialia. 61,7721-7739
Jiang, J., Britton, T., Wilkinson, A., 2013b. Measurement of geometrically necessary dislocation density with high resolution electron backscatter diffraction: Effects of detector binning and step size Ultramicroscopy 125, 1-9.
Jiang, J., Britton, T., Wilkinson, A.J., 2012. Accumulation of geometrically necessary dislocations near grain boundaries in deformed copper. Philosophical Magazine Letters, 1-9.
Kallend, J., Huang, Y., 1984. Orientation dependence of stored energy of cold work in 50% cold rolled copper. Metal science 18, 381-386.
Karamched, P.S., Wilkinson, A.J., 2010. High resolution electron back-scatter diffraction analysis of thermally and mechanically induced strains near carbide inclusions in a superalloy. ACTA MATERIALIA.59, 263-272.
Kysar, J., Saito, Y., Oztop, M., Lee, D., Huh, W., 2010. Experimental lower bounds on geometrically necessary dislocation density. International Journal of Plasticity 26, 1097-1123.
Kysar, J.W., Gan, Y.X., Morse, T.L., Chen, X., Jones, M.E., 2007. High strain gradient plasticity associated with wedge indentation into face-centered cubic single crystals: geometrically necessary dislocation densities. Journal of the Mechanics and Physics of Solids 55, 1554-1573.
Larson, B., Yang, W., Ice, G., Budai, J., Tischler, J., 2002. Three-dimensional X-ray structural microscopy with submicrometre resolution. Nature 415, 887-890.
Littlewood, P., Britton, T., Wilkinson, A., 2011. Geometrically necessary dislocation density distributions in Ti–6Al–4V deformed in tension. Acta Materialia 59, 6489-6500.
Littlewood, P., Wilkinson, A., 2012a. Geometrically necessary dislocation density distributions in cyclically deformed Ti–6Al–4V. Acta Materialia 60, 5516-5525.
Littlewood, P., Wilkinson, A., 2012b. Local deformation patterns in Ti–6Al–4V under tensile, fatigue and dwell fatigue loading. International Journal of Fatigue 43, 111-119.
Merriman, C., Field, D., Trivedi, P., 2008. Orientation dependence of dislocation structure evolution during cold rolling of aluminum. Materials Science and Engineering: A 494, 28-35.
Mishin, O.V., Godfrey, A., Jensen, D.J., 2009. Analysis of Deformation Structures in FCC Materials Using EBSD and TEM Techniques, Electron Backscatter Diffraction in Materials Science. Springer, pp. 263-275.
Nye, J., 1953. Some geometrical relations in dislocated crystals. Acta metallurgica 1, 153-162.
Pantleon, W., 2008. Resolving the geometrically necessary dislocation content by conventional electron backscattering diffraction. Scripta Materialia 58, 994-997.
Pokharel, R., Lind, J., Kanjarla, A.K., Lebensohn, R.A., Li, S.F., Kenesei, P., Suter, R.M., Rollett, A.D., 2014. Polycrystal Plasticity: Comparison Between Grain-Scale Observations of Deformation and Simulations. Annu. Rev. Condens. Matter Phys 5, 317-346.
Ruggles, T., Fullwood, D., 2013. Estimations of bulk geometrically necessary dislocation density using high resolution EBSD. Ultramicroscopy 133, 8-15.

Standard, A., 1996. E8-96a, Standard Test Methods for Tension Testing of Metallic Materials. Annual book of ASTM standards 3, 56-76.
Sun, S., Adams, B., King, W., 2000. Observations of lattice curvature near the interface of a deformed aluminium bicrystal. Philosophical Magazine A 80, 9-25.
Taylor, G., 1934. The mechanism of plastic deformation of crystals. Part I. Theoretical. Proceedings of the Royal Society of London. Series A, Containing Papers of a Mathematical and Physical Character 145, 362-387.
Wilkinson, A., Randman, D., 2010a. Determination of elastic strain fields and geometrically necessary dislocation distributions near nanoindents using electron back scatter diffraction. Philosophical Magazine 90, 1159-1177.
Wilkinson, A.J., Meaden, G., Dingley, D.J., 2006a. High-resolution elastic strain measurement from electron backscatter diffraction patterns: new levels of sensitivity. Ultramicroscopy 106, 307-313.
Wilkinson, A.J., Meaden, G., Dingley, D.J., 2006b. High resolution mapping of strains and rotations using electron backscatter diffraction. Materials Science and Technology 22, 1271-1278.
Wilkinson, A.J., Randman, D., 2010b. Determination of elastic strain fields and geometrically necessary dislocation distributions near nanoindents using electron back scatter diffraction. Philosophical Magazine 90, 1159-1177.
Zhang, Y., 1998. Solving large-scale linear programs by interior-point methods under the Matlab∗ Environment†. Optimization Methods and Software 10, 1-31.

6. Appendix:

Mathematical framework for GND density calculation

The analysis for GND content adopted in our methodology is based in Wilkinson and Randman 2010 paper on GND distribution near nanoindents (Wilkinson and Randman, 2010b).

Physical continuity is required in the displacement field, and thus integration of it over any closed loops, should result in a closure:

$$\oint_c \boldsymbol{du} = 0 \qquad \textbf{Eq.(A.1)}$$

Since $\boldsymbol{A}$ is the displacement gradient tensor and $\boldsymbol{A} = du/dx$ and thus $du = \boldsymbol{A}\, dx$. This results in Eq.(A.2):

$$\oint_c \boldsymbol{A}\, dx = 0 \qquad \textbf{Eq.(A.2)}$$

According to Stoke's theorem, the integration around C can be replaced by integration over any surface patch S bounded by C. Furthermore the displacement gradient tensor can be split into an elastic part (A^e) and a plastic part (A^p). Therefore the Eq.(A.2)can be rewritten as

$$\oiint_s curl(\boldsymbol{A})ds = \oiint_s curl(\boldsymbol{A^e} + \boldsymbol{A^p})ds = 0 \qquad \textbf{Eq.(A.3)}$$

From Eq.(A.3) we can see that over any closed loop C bounding any surface patch S, the curl of elastic displacement gradient tensor must equal to the negative curl of plastic displacement gradient tensor:

$$curl(\boldsymbol{A^e}) = -curl(\boldsymbol{A^p}) \qquad \textbf{Eq.(A.4)}$$

Within a Burgers circuit, the net Burgers vector B is defined as:

$$B = -\oint_c \boldsymbol{A^p} dx = -\oiint_S curl(\boldsymbol{A^p})ds \qquad \textbf{Eq.(A.5)}$$

And Nye's dislocation tensor $\boldsymbol{\alpha}$ is defined as(Nye, 1953):

$$\boldsymbol{B} = \oiint_s \boldsymbol{\alpha} ds \qquad \textbf{Eq.(A.6)}$$

Therefore:

$$\boldsymbol{\alpha} = -curl(\boldsymbol{A^p}) = curl(\boldsymbol{A^e}) \qquad \textbf{Eq.(A.7)}$$

The term $\boldsymbol{A^e}$ in Eq.(A.7) can be explicitly expressed in terms of individual components of the elastic strain gradient and rotation gradient, thus

$$\boldsymbol{\alpha} = \begin{pmatrix} \frac{\partial w_{12}}{\partial x_3} - \frac{\partial w_{13}}{\partial x_2} & \frac{\partial w_{13}}{\partial x_1} & \frac{\partial w_{21}}{\partial x_1} \\ \frac{\partial w_{32}}{\partial x_2} & \frac{\partial w_{23}}{\partial x_1} - \frac{\partial w_{21}}{\partial x_3} & \frac{\partial w_{21}}{\partial x_2} \\ \frac{\partial w_{32}}{\partial x_3} & \frac{\partial w_{13}}{\partial x_3} & \frac{\partial w_{31}}{\partial x_2} - \frac{\partial w_{32}}{\partial x_1} \end{pmatrix} + \begin{pmatrix} \frac{\partial \epsilon_{12}}{\partial x_3} - \frac{\partial \epsilon_{31}}{\partial x_2} & \frac{\partial \epsilon_{13}}{\partial x_1} - \frac{\partial \epsilon_{11}}{\partial x_3} & \frac{\partial \epsilon_{11}}{\partial x_2} - \frac{\partial \epsilon_{12}}{\partial x_1} \\ \frac{\partial \epsilon_{22}}{\partial x_3} - \frac{\partial \epsilon_{23}}{\partial x_2} & \frac{\partial \epsilon_{23}}{\partial x_1} - \frac{\partial \epsilon_{21}}{\partial x_3} & \frac{\partial \epsilon_{21}}{\partial x_2} - \frac{\partial \epsilon_{22}}{\partial x_1} \\ \frac{\partial \epsilon_{32}}{\partial x_3} - \frac{\partial \epsilon_{33}}{\partial x_2} & \frac{\partial \epsilon_{33}}{\partial x_1} - \frac{\partial \epsilon_{31}}{\partial x_3} & \frac{\partial \epsilon_{31}}{\partial x_2} - \frac{\partial \epsilon_{32}}{\partial x_1} \end{pmatrix} \quad \textbf{Eq.(A.8)}$$

As the HR-EBSD measurement only determine the gradients of the elastic strain and rotation in two dimensions (i.e. within the surface plane), any gradient with respect to the third direction x_3 is not accessible as highlighted (red) in

$$\boldsymbol{\alpha} = \begin{pmatrix} \frac{\partial w_{12}}{\partial x_3} - \frac{\partial w_{13}}{\partial x_2} & \frac{\partial w_{13}}{\partial x_1} & \frac{\partial w_{21}}{\partial x_1} \\ \frac{\partial w_{32}}{\partial x_2} & \frac{\partial w_{23}}{\partial x_1} - \frac{\partial w_{21}}{\partial x_3} & \frac{\partial w_{21}}{\partial x_2} \\ \frac{\partial w_{32}}{\partial x_3} & \frac{\partial w_{13}}{\partial x_3} & \frac{\partial w_{31}}{\partial x_2} - \frac{\partial w_{32}}{\partial x_1} \end{pmatrix} + \begin{pmatrix} \frac{\partial \epsilon_{12}}{\partial x_3} - \frac{\partial \epsilon_{31}}{\partial x_2} & \frac{\partial \epsilon_{13}}{\partial x_1} - \frac{\partial \epsilon_{11}}{\partial x_3} & \frac{\partial \epsilon_{11}}{\partial x_2} - \frac{\partial \epsilon_{12}}{\partial x_1} \\ \frac{\partial \epsilon_{22}}{\partial x_3} - \frac{\partial \epsilon_{23}}{\partial x_2} & \frac{\partial \epsilon_{23}}{\partial x_1} - \frac{\partial \epsilon_{21}}{\partial x_3} & \frac{\partial \epsilon_{21}}{\partial x_2} - \frac{\partial \epsilon_{22}}{\partial x_1} \\ \frac{\partial \epsilon_{32}}{\partial x_3} - \frac{\partial \epsilon_{33}}{\partial x_2} & \frac{\partial \epsilon_{33}}{\partial x_1} - \frac{\partial \epsilon_{31}}{\partial x_3} & \frac{\partial \epsilon_{31}}{\partial x_2} - \frac{\partial \epsilon_{32}}{\partial x_1} \end{pmatrix} \quad \textbf{Eq.(A.9)}$$

The inaccessible third dimension limits the number of directly determined Nye's tensor components to three of nine. However, based on our observation on our direct experimental results, it was found that the elastic strain contribution is insignificant comparing to rotation. It thus is reasonable to neglect the elastic strain part in Nye's tensor, which yields:

$$\boldsymbol{\alpha} = \begin{pmatrix} \frac{\partial w_{12}}{\partial x_3} - \frac{\partial w_{13}}{\partial x_2} & \frac{\partial w_{13}}{\partial x_1} & \frac{\partial w_{21}}{\partial x_1} \\ \frac{\partial w_{32}}{\partial x_2} & \frac{\partial w_{23}}{\partial x_1} - \frac{\partial w_{21}}{\partial x_3} & \frac{\partial w_{21}}{\partial x_2} \\ \frac{\partial w_{32}}{\partial x_3} & \frac{\partial w_{13}}{\partial x_3} & \frac{\partial w_{31}}{\partial x_2} - \frac{\partial w_{32}}{\partial x_1} \end{pmatrix} \quad \textbf{Eq.(A.10)}$$

Ignoring the elastic strain part allows five of nine Nye's tensor components to be obtained directly. In addition, as Pantleon (Pantleon, 2008) pointed out that the difference between a_{11}-a_{22} can also be obtained and used as a further constraint to improve the accuracy of estimated lower bound GND content.

The Nye's tensor relates to dislocation density ρ_s of different types of dislocations through:

$$\alpha_{ij} = \sum_{s=1}^{s_{max}} \rho_s \, b_i^s l_j^s \qquad \text{Eq. (A.11)}$$

Where $\boldsymbol{b^s}$ and $\boldsymbol{l^s}$ are the Burgers vector and unit line direction of the sth dislocation type respectively. The Eq.(A.11) can be write out more explicitly in in terms of individual components of rotation gradient, Burgers vector, line direction and dislocation density as shown in Eq.(A.12).

$$\begin{pmatrix} \alpha_{12} \\ \alpha_{13} \\ \alpha_{21} \\ \alpha_{23} \\ \alpha_{33} \\ \alpha_{11} - \alpha_{22} \end{pmatrix} = \begin{pmatrix} \frac{\partial w_{13}}{\partial x_1} \\ \frac{\partial w_{21}}{\partial x_1} \\ \frac{\partial w_{32}}{\partial x_2} \\ \frac{\partial w_{21}}{\partial x_2} \\ \frac{\partial w_{31}}{\partial x_2} - \frac{\partial w_{32}}{\partial x_1} \\ -\frac{\partial w_{13}}{\partial x_2} - \frac{\partial w_{23}}{\partial x_1} \end{pmatrix} = \begin{pmatrix} \sum_s b_1^s l_2^s \rho_s \\ \sum_s b_1^s l_3^s \rho_s \\ \sum_s b_2^s l_1^s \rho_s \\ \sum_s b_2^s l_3^s \rho_s \\ \sum_s b_3^s l_3^s \rho_s \\ \sum_s b_1^s l_1^s \rho_s - b_2^s l_2^s \rho_s \end{pmatrix} \qquad \text{Eq.(A.12)}$$

In Eq.(A.12), the $\boldsymbol{\alpha}_{ij}$ terms are generally represented by a vector $\boldsymbol{\Lambda}$ and the $\boldsymbol{A}$ is used to denote the various terms in the tensor dyadic products of the Burgers vector $\boldsymbol{b}$ and line direction $\boldsymbol{l}$ of the sth dislocation type. Therefore the Eq.(A.12) can be simply expressed as:

$$\Lambda = \boldsymbol{A\rho} \qquad \text{Eq.(A.13)}$$

It is noted that in Eq.(A.13) on the left hand side there are 6 measureable rotation gradients available whereas on the right hand side in case of FCC crystals if we only consider pure edge and pure screw dislocations, there are potentially 36 slip systems to store dislocations: a set of 12 pure screw dislocations whose Burgers vectors and line directions lie in the <110> directions, and 24 pure edge dislocations whose Burgers vectors lie in <110> directions with line directions along <112> as explored by Arsenlis and Parks(Arsenlis and Parks, 1999). Thus there is no unique solution and a set of possible combinations of slip systems can satisfy measured curvature.

In this work the more physical based L^1 optimisation scheme with line energy minimisation is used in which the solution with the least sum of dislocation line energy will be found. In our L^1 optimisation scheme all dislocations have the same Burgers vector but the energy associated with edge and screw dislocations are different according to Eq.(A.14). This L^1 optimisation scheme is implemented in Matlab (http://www.mathworks.co.uk) using the 'linprog' command (Zhang, 1998).

$$\frac{E_{edge}}{E_{screw}} = \frac{1}{1-v} \qquad \text{Eq.(A.14)}$$

Where v is the Poisson's ratio with a value of 1/3 for typical metals.